

Integrated optimization framework for multi-domain assemblies: A novel polygon topology to non-matching meshes and materials

Xinqing Li^a, Jianghong Yang^a, Mi Xiao^b, Yingjun Wang^{a,*}

^a National Engineering Research Center of Novel Equipment for Polymer Processing, The Key Laboratory of Polymer Processing Engineering of the Ministry of Education, Guangdong Provincial Key Laboratory of Technique and Equipment for Macromolecular Advanced Manufacturing, South China University of Technology, Guangzhou 510641, China

^b State Key Laboratory of Digital Manufacturing Equipment and Technology, Huazhong University of Science and Technology, Wuhan 430074, China



ARTICLE INFO

Keywords:

Optimization framework
Integrated topology
Multi-domain assembly
SBFEM
Polygonal element

ABSTRACT

Current traditional topology optimization primarily focuses on single-domain design, practical engineering structures often require multi-domain assemblies with geometric complexity, material heterogeneity, and localized load demands. This paper proposes a novel polygon topology optimization framework of assemblies, addressing the need for adaptive mesh strategies across subdomains. The proposed approach overcomes key limitations of traditional single-domain optimization by enabling seamless integration of non-matching meshes with diverse material properties through subdomain-specific discretization. The framework automatically enforces compatibility at interfaces without remeshing by utilizing S-elements of Scaled Boundary Finite Element Method (SBFEM) to connect different mesh types while maintaining equilibrium. A generalized node-to-node coupling scheme is employed to handle multi-material interfaces, accommodating both anisotropic and isotropic material combinations. The method incorporates an efficient SIMP-based optimization with subdomain-dependent volume constraint. Adaptive mesh strategies further enhance computational efficiency relative to uniform mesh method, as demonstrated in practical applications such as automotive floor frame. By eliminating ad-hoc post-processing, the framework provides a unified workflow from mesh assembly to optimized design. Numerical examples confirm the method's effectiveness in handling variable mesh densities, practical assembly constraints, and complex geometries structures.

1. Introduction

Assembly structures, comprising interconnected components designed to achieve system-level performance, are fundamental to modern engineering applications ranging from mechanical engineering [1] to building designs [2], and aerospace systems [3]. Conducting optimization design for assembly structures can effectively prevent issues of misalignment or insufficient compatibility that may arise when optimizing individual parts, and greatly meet the higher performance requirements and complex design needs. In recent years, the effective integration of topology optimization techniques with assembly structure optimization has provided a promising approach to achieving high-performance assembly structures.

Since the pioneering work of Bendsøe and Kikuchi [4], many topology optimization methods have been proposed. These include the Solid Isotropic Material with Penalization (SIMP) method [5], the

Evolutionary Structural Optimization (ESO) method [6], the Level Set Method (LSM) [7], and the Moving Morphable Component [8] (MMC) method. While traditional topology optimization has made significant strides in single-domain design, the optimization of multi-component assemblies presents unique challenges stemming from geometric complexity, material heterogeneity, and localized load demands. Current approaches to assembly optimization often either treat the system as a monolithic domain (losing component-specific design control) or optimize parts separately (risking interface incompatibilities). In early work, Jiang and Chirehdast [9] optimized the distribution of fixed geometric component connections, extending structural topology optimization to system design. Chickermane and Gea [10] proposed a model and domain definition approach to address multi-component system design, enabling structural topology optimization of interconnection locations. Li et al. [11] applied the traditional ESO method to connected components, thereby developing a comprehensive approach to

* Corresponding author.

E-mail address: wangyj84@scut.edu.cn (Y. Wang).

multi-component structural topology optimization.

The literatures [12,13] developed a method for synthesizing multi-component structural assemblies in a continuous domain, where optimized structures are automatically partitioned during the optimization process. This greatly enhances the ability to represent complex structural geometries observed in actual products. Guirguis et al. [14, 15] utilized a kriging-interpolated level set extension for multi-component topology optimization, aiming to improve optimization efficiency by reducing the number of design variables. However, these studies were based on non-gradient methods, which are considered unsuitable for topology optimization of continuum structures due to their lack of sensitivity and associated computational inefficiencies [16]. To address this, Zhou and Saitou [17] extended previous researches by proposing a gradient-based, continuously relaxed multi-component topology optimization method, achieving structural optimization of stamped sheet metal assemblies. This method was later adapted for applications in additive manufacturing (MTO-A) [18], composite materials (MTO-C) [19], die casting (MTO-D) [20], and thin-walled structural component optimization [21]. Additionally, a structural topology optimization method for the overall layout of multi-component structures [22–25] has been developed rapidly. By introducing movable components into the design domain, this method allows for the simultaneous optimization of component layout and supporting structure topology. Building on practical assembly requirements, Thomas et al. [26] incorporated common interface connection methods—such as screws, welds, or rivets—into periodic component assembly optimization. Related works include methods for the simultaneous topology optimization of parts and their connection locations [27] and sequential topology optimization for multi-component systems [28]. While these methods have shown promise in specific applications like stamped assemblies or additive manufacturing, they share a critical limitation: they assume either conforming meshes or require expensive remeshing procedures at material interfaces. This becomes particularly problematic when dealing with assemblies combining different mesh types (e.g., polygonal stress-concentration regions with quadrilateral bulk domains) or dissimilar materials (e.g., anisotropic composites joined to isotropic substrates).

These limitations become especially pronounced when addressing assemblies that combine geometrically complex components with material dissimilarities - a common scenario in modern engineering systems. Conventional approaches attempt to resolve such challenges either during optimization through domain partitioning or in post-processing through connection design, inevitably compromising either solution optimality or computational efficiency. In contrast, our framework shifts the paradigm to the pre-processing stage, where the assembly's fundamental characteristic - geometric complexity, material heterogeneity, and load requirements - can be addressed before optimization begins. At the finite element modeling stage, each component is discretized independently using subdomain-optimal meshes (e.g., polygonal elements for stress concentrations, quadrilaterals for regular regions), then assembled through a node-to-node coupling scheme [29,30] that: 1. Automatically enforces compatibility at interfaces without remeshing, 2. Preserves the local mesh fidelity of each subdomain, 3. Naturally generates polygonal transition elements at interfaces.

The geometric adaptability of polygonal elements proves particularly advantageous for optimizing complex assembly structures, where irregular component shapes and material interfaces demand flexible discretization capabilities. While conventional polygonal topology optimization relies heavily on Wachspress interpolation [31–34]. However, for implementing the polygonal finite element method (FEM), domain integration on arbitrarily shaped polygonal elements and the interpolation construction for various types of polygons are relatively complex. As a semi-analytical and semi-numerical method that does not require fundamental solutions, the scaled boundary finite element method (SBFEM) can easily analyze and solve complex polygonal

elements. Since then, researches on topology optimization based on SBFEM have largely focused on the framework of hierarchical tree mesh division. Egger et al. [35] leveraged the polyhedral characteristics of SBFEM elements on quadtree and octree meshes to address the challenges posed by hanging nodes, thereby improving computational efficiency. Zhang et al. [36] further advanced this direction by integrating the MMC method into a 3D SBFEM framework, enabling the generation of topologies with smooth and well-defined boundaries. Gao et al. [37] presented a fluid topology optimization method utilizing a quadtree SBFEM. More recently, Su et al. [38–40] introduced an SBFEM-BESO scheme driven by automatic imaging techniques, which significantly improves robustness and computational performance by investigating static analysis, dynamic behavior, and practical engineering applications. Most of the existing SBFEM-based topology optimization researches are focused solely on hierarchical tree mesh partitioning frameworks. In the context of multi-domain assembly mesh connections, the inherent characteristics of boundary discretization give SBFEM high flexibility in mesh transformation [41,42].

This study presents an integrated topology optimization framework specifically developed for assembled structures, addressing the critical challenges of multi-domain systems through a novel combination of SBFEM and SIMP methodologies. At its core, the proposed approach introduces an assembly-oriented implementation of SBFEM that directly accommodates polygonal transition elements at component interfaces while preserving mechanical equilibrium across dissimilar meshes through its boundary discretization scheme. By unifying SBFEM's polygonal element analysis capabilities with SIMP-based material distribution optimization and subdomain-dependent constraint enforcement, the framework achieves concurrent optimization of connection topology and material layout while maintaining load-path continuity across domain boundaries. Unlike conventional component-level approaches, this method treats the assembly as an integrated yet adaptable system, where each component retains its optimal discretization (polygonal or quadrilateral) while interface regions are automatically optimized as functional transition zones.

The remainder of the paper is organized as follows: Section 2 presents the mesh connection scheme for multi-domain assemblies; Section 3 introduces the fundamental concepts of SBFEM; Section 4 details the formulation and solution of the multi-domain topology optimization problem; Section 5 provides numerical examples to validate the proposed method; finally, Section 6 concludes the paper and discusses future research directions.

2. Assembly connection scheme

2.1. Multi-domain assembly diagram

The proposed assembly connection scheme establishes a novel paradigm for multi-domain topology optimization by implementing component integration at the finite element preprocessing stage. Unlike conventional approaches, which treat each component as a separate domain optimized individually during the topology optimization process and only assemble them in post-processing through Boolean operations, rigid connections, or welds—often resulting in interface discontinuities or material redundancies. Our study completes assembly connections prior to finite element modeling. The interfaces are automatically generated as transition elements by SBFEM, ensuring integrated and coordinated optimization of the entire structure.

At the core of this methodology lies a physics-aware node-to-node connection scheme that transforms traditionally problematic non-matching interfaces into optimized transition zones. As illustrated in Fig. 1, each subdomain maintains its ideal discretization pattern – whether polygonal for stress-concentrated regions, quadrilateral for regular geometries, or specialized honeycomb configurations for lightweight designs. This component-specific meshing strategy preserves local accuracy while accommodating material heterogeneity through

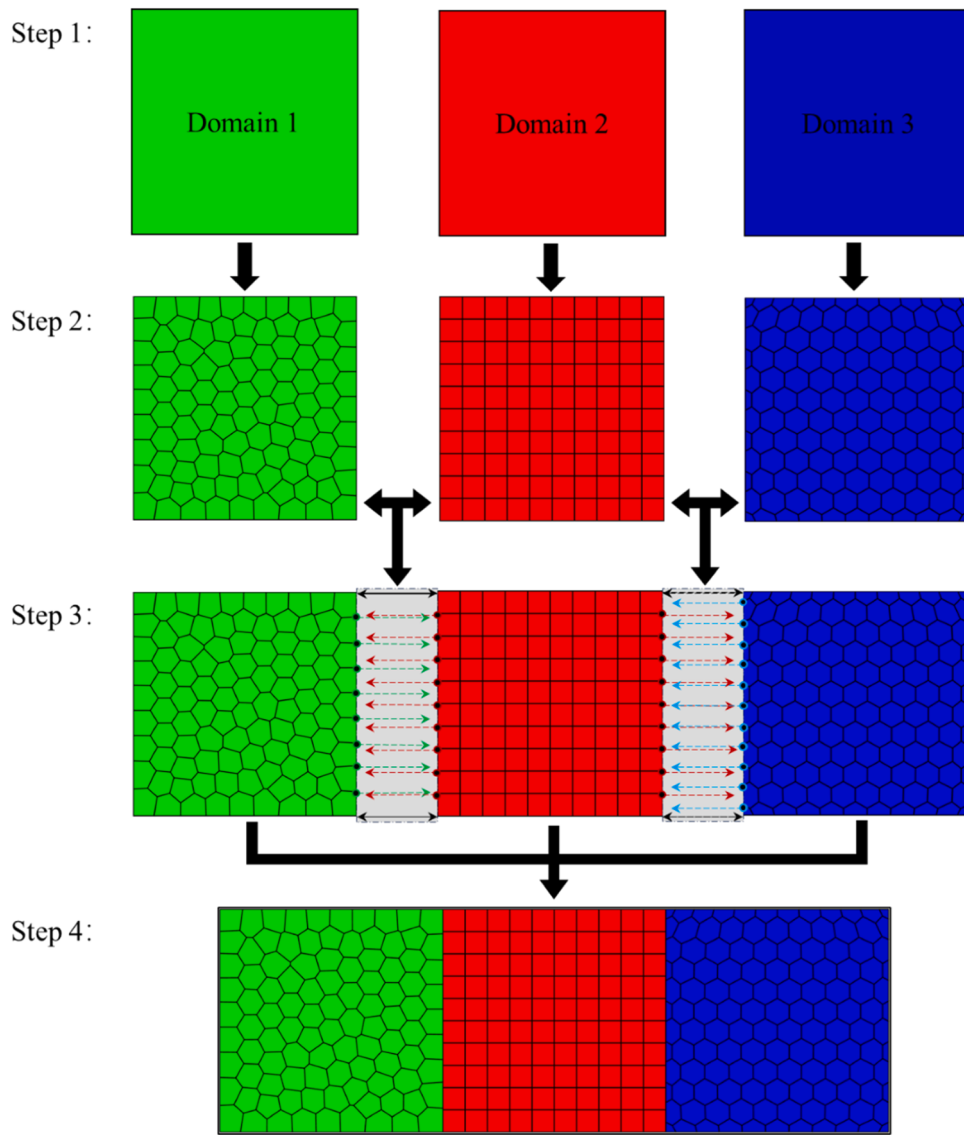


Fig. 1. Multi-domain assembly meshes connection diagram.

customized elasticity matrices for isotropic and anisotropic material assignments.

2.2. Specific implementation steps

2.2.1. Step 1: identify assembly subdomains

First, identify the components (subdomains) intended for assembly, such as Domain 1, Domain 2, and Domain 3 in the figure. Additionally, assign different material properties to each subdomain based on design requirements, represented by green, red, and blue colors in the figure for three different materials. In this study, we consider both isotropic and anisotropic materials for structural optimization. For isotropic materials, the elasticity matrix \mathbf{D} is given by:

$$\mathbf{D} = \frac{E}{1-\mu^2} \begin{bmatrix} 1 & \mu & 0 \\ \mu & 1 & 0 \\ 0 & 0 & (1-\mu)/2 \end{bmatrix} \quad (1)$$

where E is the Young's modulus, μ is Poisson's ratio.

For anisotropic materials, we use a simplified orthotropic material model [43]. In this model

$$\begin{aligned} E_1 &= E_f F_{fib} + E_m (1 - F_{fib}) \\ E_2 &= \frac{E_f E_m}{E_m F_{fib} + E_f (1 - F_{fib})} \\ G_{12} &= \frac{G_f G_m}{G_m F_{fib} + G_f (1 - F_{fib})} \\ \mu_{12} &= \mu_f F_{fib} + \mu_m (1 - F_{fib}) \\ \mu_{21} &= \mu_{12} \frac{E_2}{E_1} \end{aligned} \quad (2)$$

where E_f , μ_f and G_f represent the Young's modulus, Poisson's ratio, and shear modulus of the reinforcing material, respectively. E_m , μ_m and G_m represent the Young's modulus, Poisson's ratio, and shear modulus of the matrix material, respectively. F_{fib} represents the fiber volume fraction. The elasticity of anisotropic material model can be expressed as:

$$\mathbf{D} = \begin{bmatrix} \frac{E_1}{1 - \mu_{12}\mu_{21}} & \frac{E_1\mu_{21}}{1 - \mu_{12}\mu_{21}} & 0 \\ \frac{E_1\mu_{21}}{1 - \mu_{12}\mu_{21}} & \frac{E_2}{1 - \mu_{12}\mu_{21}} & 0 \\ 0 & 0 & G_{12} \end{bmatrix} \quad (3)$$

2.2.2. Step 2: construct mesh models

Each subdomain identified in Step 1 undergoes independent meshing. Any displacement-based polygonal element type is feasible. This paper provides three mesh types: non-uniform polygonal mesh, quadrilateral mesh, and approximated polygonal mesh with honeycomb feature, as shown in Fig. 2. Where Mesh 1 is primarily generated using the PolyMesher tool [44], which combines Voronoi partitioning with a boundary optimization strategy to ensure boundary conformity and internal quality. In addition, the Mesh 3 is constructed by connecting the centroids of a regular triangulation [45]. Different mesh types can significantly meet the needs of engineering design and analysis, especially for design domains with complex boundaries. Mesh types 1 and 3 are particularly effective in achieving accurate domain discretization.

2.2.3. Step 3: multi-domain mesh connection

The connection process begins with precise geometric parameterization of interface boundaries (Fig. 3a), where nodal compatibility is established through parametric coordinate matching. Boundary nodes from adjacent subdomains are intelligently merged, with new transition nodes inserted only where necessary to maintain mesh quality. The scheme's true innovation emerges in its automatic generation of polygonal S-elements at these junctions, leveraging SBFEM's inherent flexibility to create mechanically sound transitions between dissimilar meshes [38,39]. This process naturally handles challenging scenarios such as quadrilateral-to-polygonal connections or mixed material interfaces without artificial stiffness penalties.

Fig. 3(a) illustrates a straight line defined by two boundary nodes. The origin of the coordinate system is set at Point A, and the distance between Points A and B is denoted as $\sqrt{x_B^2 + y_B^2}$. Considering a query point, such as Point C, the twice the area of the triangle formed by Points A, B and C equal $|x_{CYB} - y_{CXB}|$. When the height of the triangle is zero, the point (i.e., the boundary node of the other domain mesh) lies on the line.

Furthermore, the two meshes are connected at the interface, and duplicate nodes are removed to generate the Multi-domain mesh. Based on this, the node indices are reassigned. Fig. 3(b) demonstrates the process of connecting the boundaries of the two domain meshes and shows the boundary element node indices of Mesh (a) and Mesh (b). Where Mesh (a) is: {[122, 123, 144, 143, 121], [142, 143, 144, 161, 160]} and Mesh (b) is: {[91, 90, 100, 101]}. After mesh connection, the element indices become: {[186, 196, 197, 198, 182, 173], [182, 198, 199, 200, 184, 174], [197, 214, 215, 199, 198]}.

2.2.4. Step 4: obtain the assembly mesh model

Following Step 3, boundary nodes are inserted into the interface of the adjacent subdomain. The line elements along the interface are then divided by the new nodes into two shorter line segments, which serve as new boundary edges for the redefined polygonal elements, as illustrated in Fig. 3(c). The resulting assembly maintains all component-specific mesh advantages while functioning as a unified computational model.

Crucially, the assembled structure preserves key features for subsequent topology optimization, including clear material interfaces, consistent load paths, and adaptable boundary conditions. And it eliminates the computational overhead of iterative remeshing while avoiding the artificial stiffness common in post-processed assemblies. Most importantly, it provides the foundation for integrated topology optimization where both material distribution and connection topology evolve simultaneously during the design process - a capability demonstrated in Section 4's SBFEM-SIMP implementation.

3. Solving polygon element based on SBFEM

3.1. Problem description

The essence of the assembly connection proposed in this paper is to transform independent single-domain meshes into multi-domain compatible meshes. Initially, the independent meshes are incompatible because displacement continuity cannot be enforced at the nodes. However, using the S-elements of SBFEM, the meshes can be modified to match at their interfaces. Once converted to a compatible polygonal mesh, the system can be readily solved using SBFEM, provided a scaling condition is met (i.e., the scaling center must be visible across the boundary). It is important to note that this study focuses on linear elasticity.

The two-dimensional linear elasticity problem [42], a typical boundary value problem in mechanics, is governed by three control equations: the physical equation, the geometric equation, and the equilibrium equation. In vector form, these equations can be expressed as follows:

$$\begin{cases} \sigma = D\epsilon \\ \epsilon = Lu \quad \text{in } \Omega \\ L^T \sigma + \bar{f} = 0 \end{cases} \quad (4)$$

where σ represents the stress field, D is the elasticity matrix, ϵ represents the strain field, L represents the strain-displacement matrix, \bar{f} represents the body force vector.

3.2. Scaled boundary finite element solution

As a semi-analytical, semi-numerical boundary element method, the SBFEM was first introduced by Song and Wolf [46]. SBFEM combines the characteristics of the finite element method without fundamental solutions and the boundary element method with dimension reduction, making it well-suited for solving problems with polygonal elements.

Consider an example of boundary-connected elements, as illustrated in Fig. 4. Here, each element is treated as a scaled boundary finite element. In the figure, O represents the scaling center, which in this study is defined as the centroid of the polygonal element. Lines extending from the scaling center to each edge of the polygon create subdomains, as shown in Fig. 4(b). These subdomains can be described

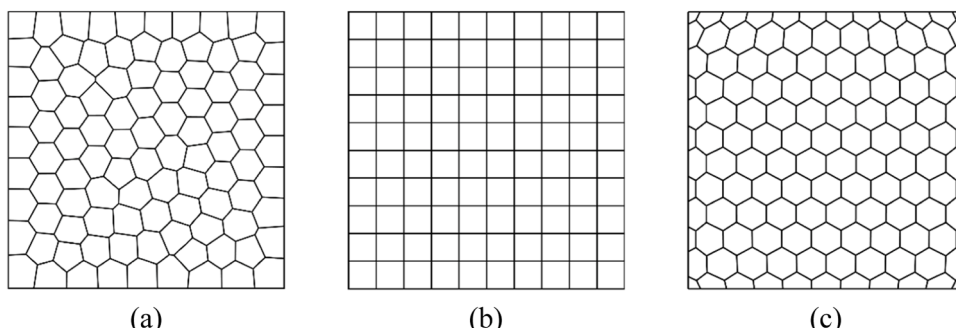


Fig. 2. Mesh types, (a) non-uniform polygonal mesh, (b) quadrilateral mesh, (c) approximated polygonal mesh with honeycomb feature.

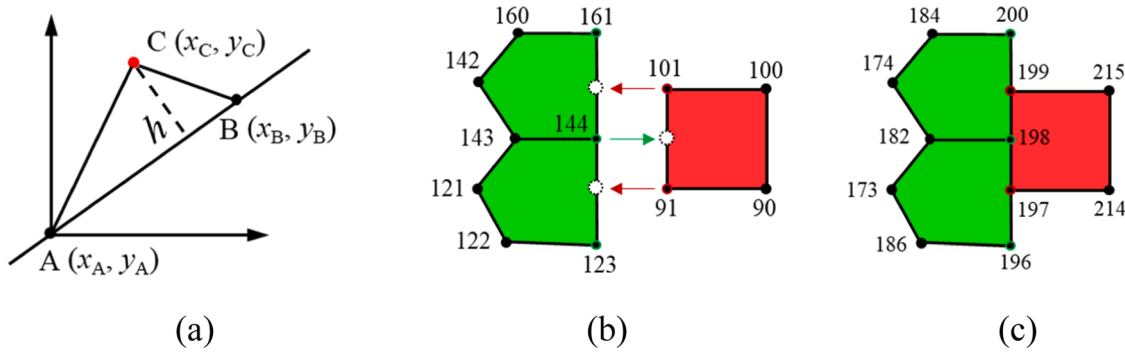


Fig. 3. Connection details of boundary elements, (a) find point on line, (b) before connection, (c) after connection.

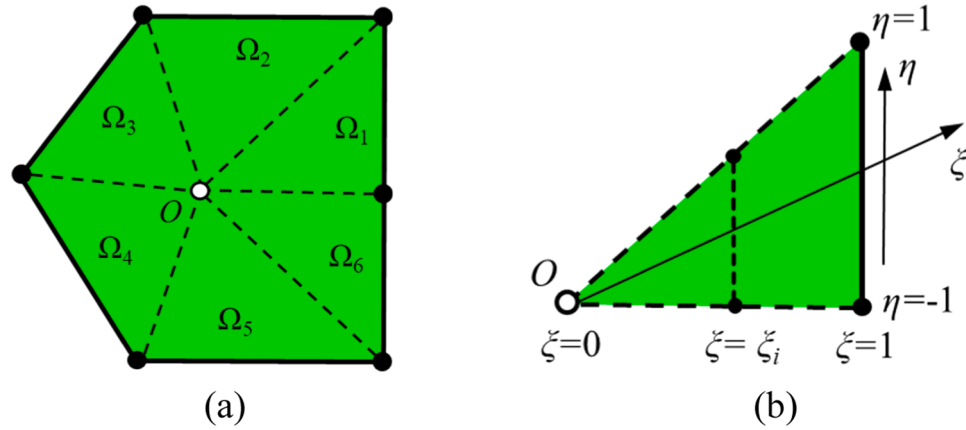


Fig. 4. Scaled boundary polygon, (a) S-domain, (b) subdomain.

using scaled boundary coordinates (ξ, η) , where ξ denotes the radial coordinate, ranging from 0 at the scaling center to 1 at the boundary, and η denotes the circumferential coordinate, with a range of $[-1, 1]$.

To solve the aforementioned element, we first need to perform a coordinate transformation, specifically from Cartesian coordinates to scaled boundary coordinates [47]. The coordinates (x, y) of any point within the domain can then be expressed as:

$$\begin{aligned} x &= x_0 + \xi \mathbf{N}(\eta) \mathbf{x} \\ y &= y_0 + \xi \mathbf{N}(\eta) \mathbf{y} \end{aligned} \quad (5)$$

where (x_0, y_0) represents the coordinates of the scaling center, while \mathbf{x} and \mathbf{y} are vectors denoting the coordinates of the nodes on the boundary. The term $\mathbf{N}(\eta)$ represents a one-dimensional shape function, defined as $\mathbf{N} = [N_1 \ N_2] = [(1-\eta)/2 \ (1+\eta)/2]$.

According to the principle of virtual work, and disregarding body forces, the equilibrium condition is given by:

$$\int_V \delta \epsilon(\xi, \eta)^T \sigma(\xi, \eta) dV - \int_V \delta u(\eta)^T t(\eta) dS \quad (6)$$

where $\delta \epsilon$ denotes the virtual strain, δu denotes the virtual displacement, and t represents the boundary traction.

This equation can be further simplified as follows:

$$\begin{aligned} \delta u_b^T (\mathbf{E}_0 u(\xi)_{,\xi} + \mathbf{E}_1^T u(\xi)|_{\xi=1}) - \delta u_b^T \mathbf{p} \\ - \int_0^1 \delta u(\xi)^T \left(\mathbf{E}_0 \xi^2 u(\xi)_{,\xi\xi} + (\mathbf{E}_0 + \mathbf{E}_1^T - \mathbf{E}_1) u(\xi)_{,\xi} - \mathbf{E}_2 \frac{1}{\xi} u(\xi) \right) d\xi = 0 \end{aligned} \quad (7)$$

where \mathbf{u}_b and \mathbf{p} represent the nodal displacements and equivalent nodal forces on the boundary, respectively. The terms \mathbf{E}_0 , \mathbf{E}_1 and \mathbf{E}_2 denote the coefficient matrices, defined as follows:

$$\begin{aligned} \mathbf{E}_0 &= \int_{\partial\Omega} \mathbf{B}_1(\eta)^T \mathbf{D} \mathbf{B}_1(\eta) |\mathbf{J}| d\eta \\ \mathbf{E}_1 &= \int_{\partial\Omega} \mathbf{B}_2(\eta)^T \mathbf{D} \mathbf{B}_1(\eta) |\mathbf{J}| d\eta \\ \mathbf{E}_2 &= \int_{\partial\Omega} \mathbf{B}_2(\eta)^T \mathbf{D} \mathbf{B}_2(\eta) |\mathbf{J}| d\eta \end{aligned} \quad (8)$$

where \mathbf{B}_1 and \mathbf{B}_2 represent the strain and displacement relationship, defined as:

$$\begin{aligned} \mathbf{B}_1(\eta) &= \frac{1}{|\mathbf{J}|} \begin{bmatrix} y(\eta)_{,\eta} & 0 \\ 0 & -x(\eta)_{,\eta} \\ -x(\eta)_{,\eta} & y(\eta)_{,\eta} \end{bmatrix} \mathbf{N}_u(\eta) \\ \mathbf{B}_2(\eta) &= \frac{1}{|\mathbf{J}|} \begin{bmatrix} -y(\eta) & 0 \\ 0 & x(\eta) \\ x(\eta) & -y(\eta) \end{bmatrix} \mathbf{N}_u(\eta) \end{aligned} \quad (9)$$

where \mathbf{N}_u is the interpolation function, defined as $\mathbf{N}_u = [\mathbf{N}_1 \mathbf{I}_{2 \times 2} \ \mathbf{N}_2 \mathbf{I}_{2 \times 2}]$, $\mathbf{I}_{2 \times 2}$ represents the 2×2 identity matrix. The Jacobian matrix \mathbf{J} is defined as:

$$\mathbf{J} = \begin{bmatrix} x(\eta) & y(\eta) \\ x(\eta)_{,\eta} & y(\eta)_{,\eta} \end{bmatrix} \quad (10)$$

According to Eq. (6), we obtain the required scaled boundary finite element equation as:

$$\mathbf{E}_0 \xi^2 u(\xi)_{,\xi\xi} + (\mathbf{E}_0 + \mathbf{E}_1^T - \mathbf{E}_1) u(\xi)_{,\xi} - \mathbf{E}_2 \frac{1}{\xi} u(\xi) = 0 \quad (11)$$

By transforming the second-order differential equation into a first-order differential equation, we obtain a differential equation

$$\xi \begin{Bmatrix} \mathbf{u}(\xi) \\ \mathbf{q}(\xi) \end{Bmatrix}_{,\xi} = \mathbf{Z} \begin{Bmatrix} \mathbf{u}(\xi) \\ \mathbf{q}(\xi) \end{Bmatrix} = \begin{bmatrix} -\mathbf{E}_0^{-1}\mathbf{E}_1^T & \mathbf{E}_0^{-1} \\ \mathbf{E}_2 - \mathbf{E}_1\mathbf{E}_0^{-1}\mathbf{E}_1^T & \mathbf{E}_1\mathbf{E}_0^{-1} \end{bmatrix} \begin{Bmatrix} \mathbf{u}(\xi) \\ \mathbf{q}(\xi) \end{Bmatrix} \quad (12)$$

where \mathbf{Z} is the Hamiltonian coefficient matrix, which facilitates the use of eigenvalue decomposition for improved computational efficiency and stability. This approach provides a semi-analytical solution for each polygonal element, significantly reducing the time required for stiffness matrix assembly, and is particularly well-suited for unstructured polygonal meshes. Furthermore, it can be decoupled into pairs of eigenvalues using an eigenvalue decomposition as

$$\mathbf{Z}\Phi = \mathbf{Z} \begin{bmatrix} \Phi_n^u & \Phi_p^u \\ \Phi_n^q & \Phi_p^q \end{bmatrix} = \begin{bmatrix} \Phi_n^u & \Phi_p^u \\ \Phi_n^q & \Phi_p^q \end{bmatrix} \begin{bmatrix} \Lambda_n & \\ & \Lambda_p \end{bmatrix} \quad (13)$$

where, Φ is a transformation matrix with independent column vectors, Λ_n and Λ_p contain the eigenvalues with negative and positive real parts resulting from the eigenvalue decomposition, representing solutions for bounded and unbounded fields, respectively. The eigenvalues are sorted in ascending order based on their real parts. Correspondingly, the eigenvectors are partitioned in a similar manner, where the submatrices Φ_n^u and Φ_p^q associated with the bounded domain solution.

Using Eq. (12), the solution to Eq. (11) can then be expressed as:

$$\begin{aligned} \mathbf{u}(\xi) &= \Phi_n^u \xi^{-\Lambda_n} \mathbf{c} \\ \mathbf{q}(\xi) &= \Phi_n^q \xi^{-\Lambda_n} \mathbf{c} \end{aligned} \quad (14)$$

where, \mathbf{c} represents the integration constant, which are determined based on the boundary conditions and can be defined by the nodal displacements $\mathbf{u}_b = \mathbf{u}(\xi)|_{\xi=1}$ on the polygon boundary

$$\mathbf{c} = (\Phi_n^u)^{-1} \mathbf{u}_b \quad (15)$$

Further, the stiffness matrix for the polygonal element can be obtained as follows:

$$\mathbf{k} = \Phi_n^q (\Phi_n^u)^{-1} \quad (16)$$

4. Topology optimization for multi-domain

4.1. Material selection

For topology optimization, selecting appropriate materials is crucial, as different material properties influence structural performance. Building upon the assembly connection scheme established in Section 2, each subdomain maintains independent material definitions while participating in the unified optimization process. The framework accommodates both isotropic and anisotropic material models through customized elasticity matrices. This material flexibility enables targeted property assignment to different assembly components while ensuring mechanical consistency at interfaces through the SBFEM formulation.

4.2. SBFEM-SIMP optimization framework

The proposed multi-domain topology optimization framework integrates SBFEM with SIMP approach to address the unique challenges of assembled structures. This methodology extends conventional topology optimization by simultaneously considering three critical aspects: (1) subdomain-specific material properties, (2) interface compatibility, and (3) global structural performance. The relationship between the material's elastic modulus and density is given by:

$$E_d(x_i) = E_{\min,d} + \tilde{x}_{i,d}^\rho (E_d - E_{\min,d}) \quad (17)$$

where, $E_{\min,d}$ represents the elastic modulus of a low-stiffness material element in d subdomain, and ρ is the penalty factor. The element density, denoted as $\tilde{x}_{i,d}$, can be defined:

$$\tilde{\mathbf{x}}_d = \mathbf{H}\mathbf{x}_d \quad (18)$$

where $\tilde{\mathbf{x}}_d$ and \mathbf{x}_d represent the density vectors before and after filtering in d subdomain, respectively. \mathbf{H} denotes the filter matrix, which is defined as:

$$\mathbf{H} = \frac{\max(0, |\Omega_{i,d}|(1 - |\mathbf{x}_{j,d} - \mathbf{x}_{i,d}|/R))}{\sum_{k \in S(j)} |\Omega_{i,d}|(1 - |\mathbf{x}_{j,d} - \mathbf{x}_{i,d}|/R)} \quad (19)$$

where, $S(j)$ denotes the set of neighboring elements for element $\Omega_{i,d}$, $\mathbf{x}_{j,d}$ and $\mathbf{x}_{i,d}$ represent the centroids of elements, respectively. R is the filter radius.

The topology optimization problem, aimed at minimizing structural compliance with a volume constraint, can be formulated as follows:

$$\begin{aligned} \text{Min}_x : \mathbf{C}(\mathbf{x}, \mathbf{u}) &= \mathbf{f}^T \mathbf{u} \\ \text{s.t.} : g &= \frac{\sum v_{i,d} \tilde{x}_{i,d}}{\sum v_{i,d}} - V_f \\ \mathbf{K}(\mathbf{x}) \mathbf{u} &= \mathbf{f} \end{aligned} \quad (20)$$

where, \mathbf{f} and \mathbf{u} represent the load and displacement vectors, respectively. \mathbf{K} is the global stiffness matrix, and $v_{i,d}$ is the volume of element i .

In the context of topology optimization, sensitivity analysis is critical to determining how the objective function changes with respect to the design variable x . For the assembly structure optimization, sensitivity analysis is used to evaluate how variations in the density field impact the structural compliance. The derivative of structural compliance with respect to the design variables is given by

$$\frac{\partial \mathbf{C}}{\partial \mathbf{x}} = \frac{\partial \mathbf{C}}{\partial \tilde{\mathbf{x}}} \frac{\partial \tilde{\mathbf{x}}}{\partial \mathbf{x}} = -\mathbf{H}^T \sum_{d=1}^{md} \sum_{i=1}^{mi} \mathbf{x}_d \tilde{x}_{i,d}^{\rho-1} \mathbf{u}_{i,d}^T (\Phi_n^q (\Phi_n^u)^{-1})_{i,d} \mathbf{u}_{i,d} \quad (21)$$

where md and mi are the number of subdomains and the number of subdomain elements respectively. And the partial derivative of the volume with respect to the design variables is:

$$\frac{\partial g}{\partial \mathbf{x}} = \mathbf{H}^T \mathbf{V} \left/ \sum_{d=1}^{md} \sum_{i=1}^{mi} v_{i,d} \right. \quad (22)$$

where \mathbf{V} represents element volume vector.

4.3. Design variable update

In topology optimization, design variables need to be updated in order to iteratively optimize the structure's shape and material distribution. For assembly structures, the update of design variables enables the collaborative optimization of individual parts within the assembly, allowing the overall system's strength, stiffness, and stability to reach optimal levels under the best material and structural distribution. This paper uses the optimization criterion (OC) method [31] mentioned in reference for updating the design variables.

$$x_{i,d}^* = x_{\min,d} + \left(\frac{-\frac{\partial f}{\partial x_{i,d}} \Big|_{x=x^0}}{\lambda \frac{\partial g}{\partial x_{i,d}} \Big|_{x=x^0}} \right)^{\frac{1}{1-\alpha}} (x_{i,d}^0 - x_{\min,d}) \quad (23)$$

where the "reciprocal" variable α is taken as -1 . Note that the update of the design variables depends on the associated Lagrange multiplier λ , and needs to be controlled within the following constraints using the upper and lower limits ($x_{\max,d}$, $x_{\min,d}$) of the density variable:

$$x_{i,d}^{\text{new}} = \begin{cases} x_{i,d}^+, x_{i,d}^* \geq x_{i,d}^+ \\ x_{i,d}^-, x_{i,d}^* \geq x_{i,d}^- \\ x_{i,d}^*, \text{otherwise} \end{cases} \quad (24)$$

where $x_{i,d}^+$ and $x_{i,d}^-$ are the boundaries of the search region, given by the following equation:

$$x_{i,d}^+ = \max(x_{\max,d}, x_{i,d}^0 + \delta), x_{i,d}^- = \max(x_{\max,d}, x_{i,d}^0 - \delta) \quad (25)$$

Additionally, the conventional OC method is not applicable for multi-constraint problem. As an extension of the OC framework, ZPR optimization scheme [48], addresses this limitation by leveraging the separability of the dual problem of a convex approximated atomic subproblem with respect to the Lagrange multipliers. This allows the update of design variables under each volume constraint to depend solely on its corresponding multiplier. The detailed implementation of this method for polygonal topology can be found in Reference [33] and is therefore not repeated here.

5. Numerical examples

5.1. Infinite plane with a hole

This benchmark study provides essential validation of our assembly framework's core capability to maintain mechanical accuracy across connected subdomains. Computation is performed on a PC with 12th Gen Intel(R) Core (TM) i7-12700F 2.10 GHz CPU and 16 GB RAM. An infinite plane with a radius $r = 0.4$ m hole is subjected to remote uniaxial uniform tension $p = 1$ kPa. The displacement analytical solution for this problem is expressed in polar coordinates (α, θ) as follows:

$$\begin{aligned} u_x &= \frac{pr}{8G} \left[\frac{\alpha}{r} (1 + \kappa) \cos \theta + \frac{2r}{\alpha} ((1 + \kappa) \cos \theta + \cos 3\theta) - \frac{2r^3}{\alpha^3} \cos 3\theta \right] \\ u_y &= \frac{pr}{8G} \left[\frac{\alpha}{r} (\kappa - 3) \sin \theta + \frac{2r}{\alpha} ((1 - \kappa) \sin \theta + \sin 3\theta) - \frac{2r^3}{\alpha^3} \sin 3\theta \right] \end{aligned} \quad (26)$$

Where κ is the Kolosov constant, defined as

$$\kappa = \begin{cases} \frac{3 - \mu}{1 + \mu} \text{ for plane stress} \\ 3 - 4\mu \text{ for plane strain} \end{cases} \quad (27)$$

To model this problem, we approximate the infinite plate with a circular hole by substituting it with two rectangular domains above and below the hole, each with dimensions of 2 m \times 1 m. The exact displacement solution at the hole's edge is used as the boundary condition along the four sides of the resulting square when the two rectangular domains are connected, as shown in Fig. 5. Additionally, the Young's modulus for both domains is set to 10^3 kPa.

First, the mesh is generated separately for the assumed regions above and below the circular hole, as shown in Fig. 6(a) and Fig. (b). Fig. 6(c)

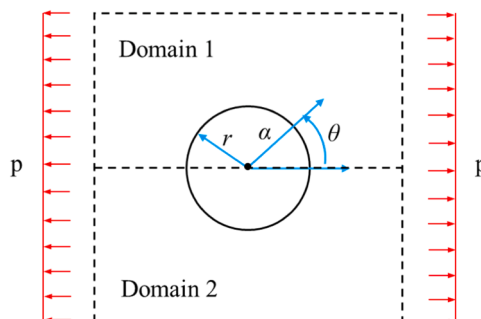


Fig. 5. Illustration of the infinite plate with a circular hole.

displays the multi-domain mesh model created by connecting these two domains. To better observe the boundary connection method, the corresponding element nodes and boundary nodes (indicated by black circles) are highlighted. We also present the deformed displacement contour plot in Fig. 6(d). For comparison, we consider a single-domain mesh of the infinite plate under the same settings, as shown in Fig. 7, which includes both the mesh and the displacement contour plot. From the displacement contours, it can be observed that due to the influence of the boundary mesh connection, there are slight differences in the displacement distribution between the multi-domain and single-domain contour plots.

To further investigate the impact of multi-domain and single-domain meshes on solution accuracy, we introduce the relative displacement error norm (N_{rde}) for verification, which is mathematically expressed as:

$$N_{rde} = \frac{\|\mathbf{u}^{exa} - \mathbf{u}\|}{\|\mathbf{u}^{exa}\|} \quad (28)$$

where \mathbf{u}^{exa} and \mathbf{u} represent the analytical and numerical displacement solutions, respectively. The displacement error norm for both mesh types (polygonal elements) under different degrees of freedom is presented in Table 1, and the corresponding comparison curve is shown in Fig. 8. From the results, it can be seen that the displacement accuracy of the multi-domain mesh is slightly lower than that of the single-domain mesh, but still achieves a good level of solution accuracy. The results demonstrate that our node-to-node coupling scheme introduces only marginal accuracy loss while preserving critical load paths. These results establish two critical foundations for subsequent engineering applications: (1) quantified verification of assembly accuracy, (2) demonstration of uninterrupted load path continuity.

5.2. Corbel beam

This example mainly validates the feasibility of topology optimization for multi-domain assembly-connected structures. To achieve this, we investigate the problem from two aspects: multi-domain connection mode, and mesh type for connection. First, we present the single-domain corbel beam with its corresponding quadrilateral mesh, optimized topology and compliance as shown in Fig. 9. Where the design domain, boundary conditions, and load conditions are visually displayed in Fig. 9 (a). In this study, different subdomains use the same isotropic material, with a Young's modulus of 1 and a Poisson's ratio of 0.3. The beam has a length of $L = 2$, with the top and bottom fixed and a downward force of magnitude 1.5 applied at the right end. The filter radius is set to 0.15, and the volume fraction is set to 0.25.

5.2.1. Multi-domain connection mode

Fig. 10 shows four different assembly connection modes, including: Mode 1 (Assembly of Domain 1 with 500 elements, Domain 2 with 500 elements, Domain 3 with 500 elements, Domain 4 with 500 elements), Mode 2 (Assembly of Domain 1 with 1500 elements and Domain 2 with 500 elements), Mode 3 (Assembly of Domain 1 with 500 elements, Domain 2 with 1000 elements, and Domain 3 with 500 elements) and Mode 4 (Assembly of Domain 1 with 1000 elements, Domain 2 with 500 elements, and Domain 3 with 500 elements). First, the subdomains are determined, and their mesh discretization is carried out. Then, based on the design requirements, the subdomains are connected, resulting in the mesh discretization of the multi-domain assembly structure, as shown in Fig. 11.

Further, based on the above mesh discretization, structural topology optimization is performed on the assembled multi-domain structure, yielding the corresponding topological configurations and structural compliances shown in Fig. 12. The results demonstrate that performing topology optimization on multi-domain assembly connections is feasible.

The corbel beam example systematically evaluates four distinct

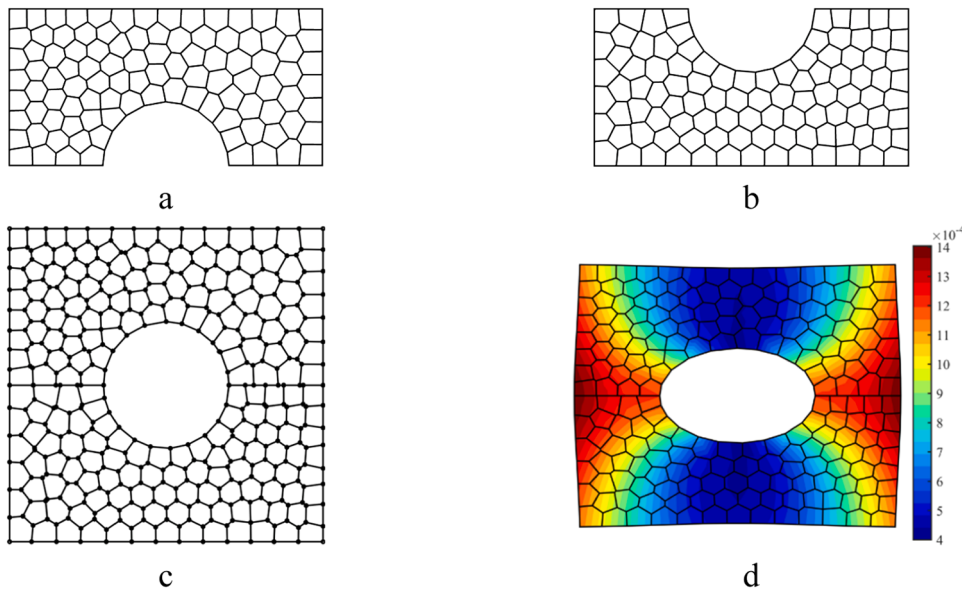


Fig. 6. Mesh discretization of the multi-domain. (a) Domain 1, (b) Domain 2, (c) Connected domains, (d) Displacement contour plot.

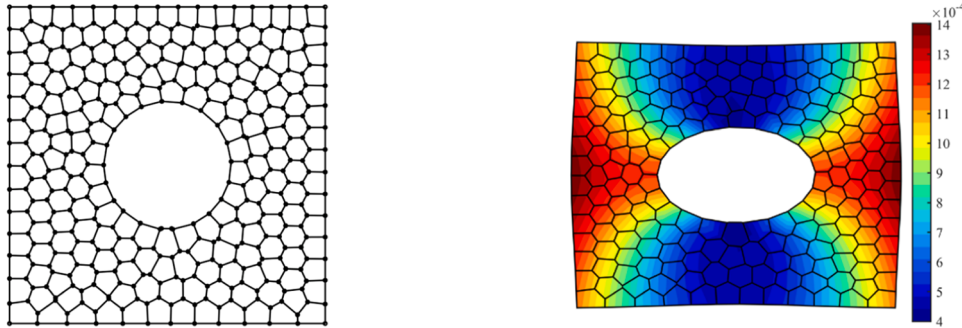


Fig. 7. Single-domain. (a) Mesh discretization, (b) Displacement contour plot.

Table 1

Relative displacement error norm for multi-domain and single-domain mesh discretization.

Multi-domain			Single-domain		
Element numbers	DOF	N_{rde}	Element numbers	DOF	N_{rde}
200	806	3.01E-3	200	812	2.91E-3
600	2402	9.21E-4	600	2400	8.51E-4
1200	4788	4.24E-4	1200	4800	4.07E-4
2400	9558	1.94E-4	2400	9594	1.86E-4
4800	19,182	8.90E-5	4800	9584	8.61E-5

assembly configurations with varying subdomain divisions and element distributions. The optimized results demonstrate remarkable consistency in structural performance, with compliance values under the four modes showing relative errors of only 1.017 %, 0.468 %, 0.173 %, and 0.096 %, respectively, compared to the baseline single-domain configuration (Fig. 9(c)) with a compliance of 155.98. These confirm the framework's robustness to different connection schemes while maintaining optimal load paths. Notably, the material distributions show only localized differences at interfaces without compromising global structural integrity, proving the method's ability to adapt to diverse assembly requirements.

5.2.2. Multi-domain mesh types

In this example, we focus on the structural topology optimization of

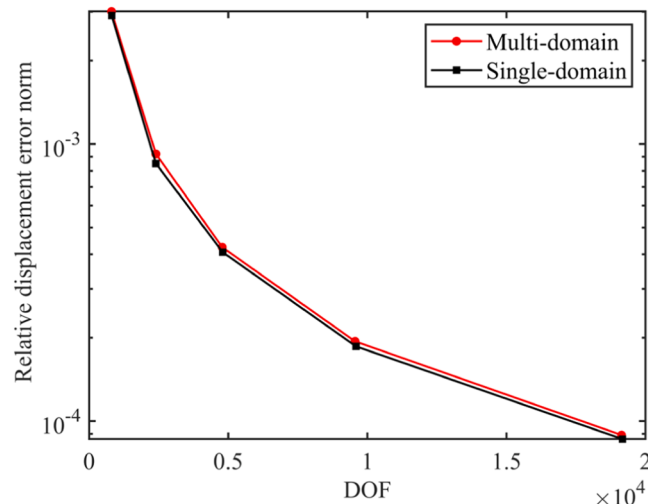


Fig. 8. Comparison curve of N_{red} between multi-domain and single-domain mesh discretization.

multi-domain mesh connections for different domain mesh types. The mesh types selected are the three types shown in Fig. 2. The mesh connection method follows the approach in Figs. 10(a) and (b), where the number of elements per unit area is kept approximately the same.

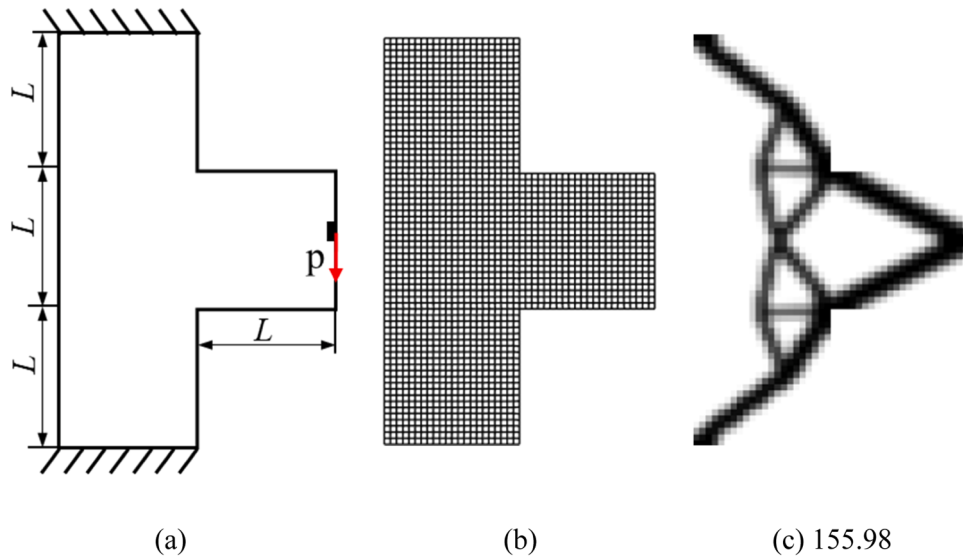


Fig. 9. Single-domain corbel beam, (a) schematic diagram, (b) quadrilateral mesh, (c) topology configuration.

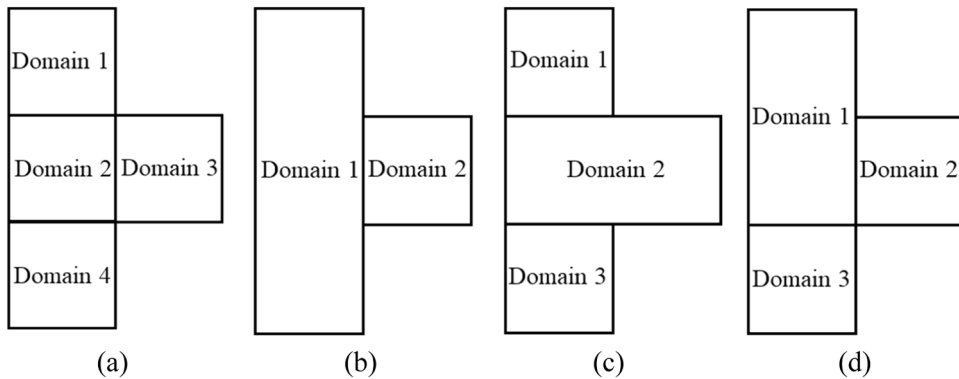


Fig. 10. Assembly connection mode, (a) Mode 1, (b) Mode 2, (c) Mode 3, (d) Mode 4.

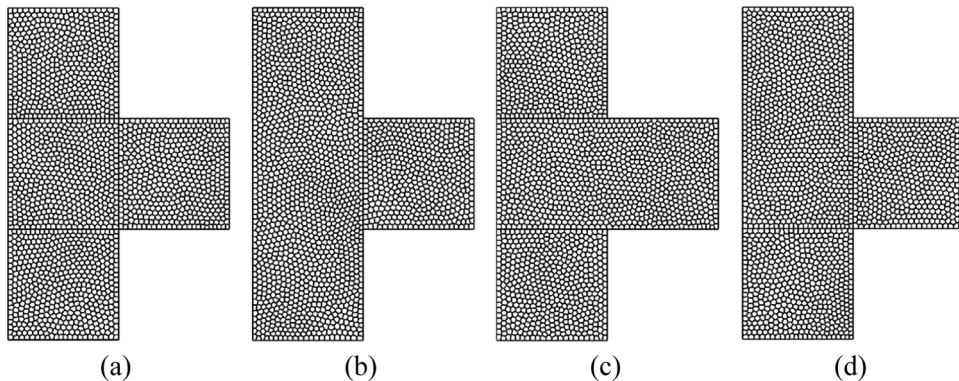


Fig. 11. Mesh connection of the assembled multi-domain structure, (a) Mode 1, (b) Mode 2, (c) Mode 3, (d) Mode 4.

Figs. 13(a) and (b) show the multi-domain mesh discretization after assembly connection. To facilitate observation of the connection details, enlarged images of the corners are provided. It can be observed that even with different types of meshes, the subdomains can still be well-connected, further confirming that this mesh connection method has good applicability. Based on this assembly connection, corresponding topological configurations are generated as shown in Fig. 13(c) and Fig. 13(d).

The example further verifies the framework's unique capability to

handle heterogeneous mesh combination. Three fundamentally different mesh types - including irregular polygons and structured quadrilaterals - are successfully integrated while preserving: (1) interface stress continuity, (2) geometric compatibility, and (3) optimization convergence. The resulting topologies exhibit smooth material transitions across mesh boundaries. This flexibility is particularly valuable for practical engineering where components often require different discretization strategies.

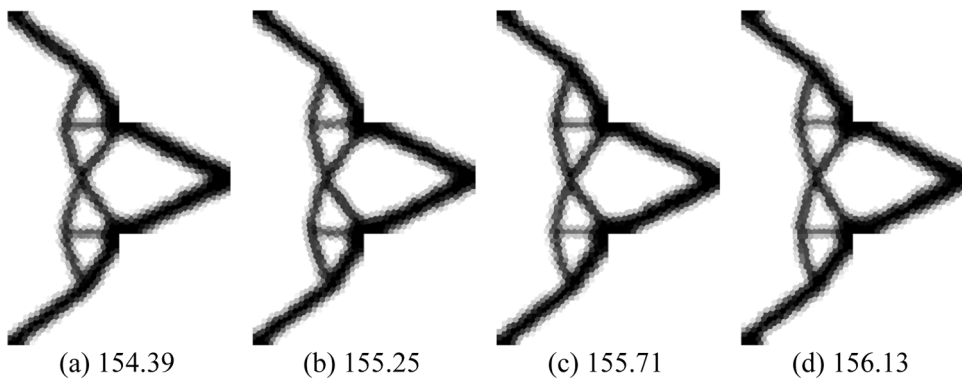


Fig. 12. Topological configurations, (a) Mode 1, (b) Mode 2, (c) Mode 3, (d) Mode 4.

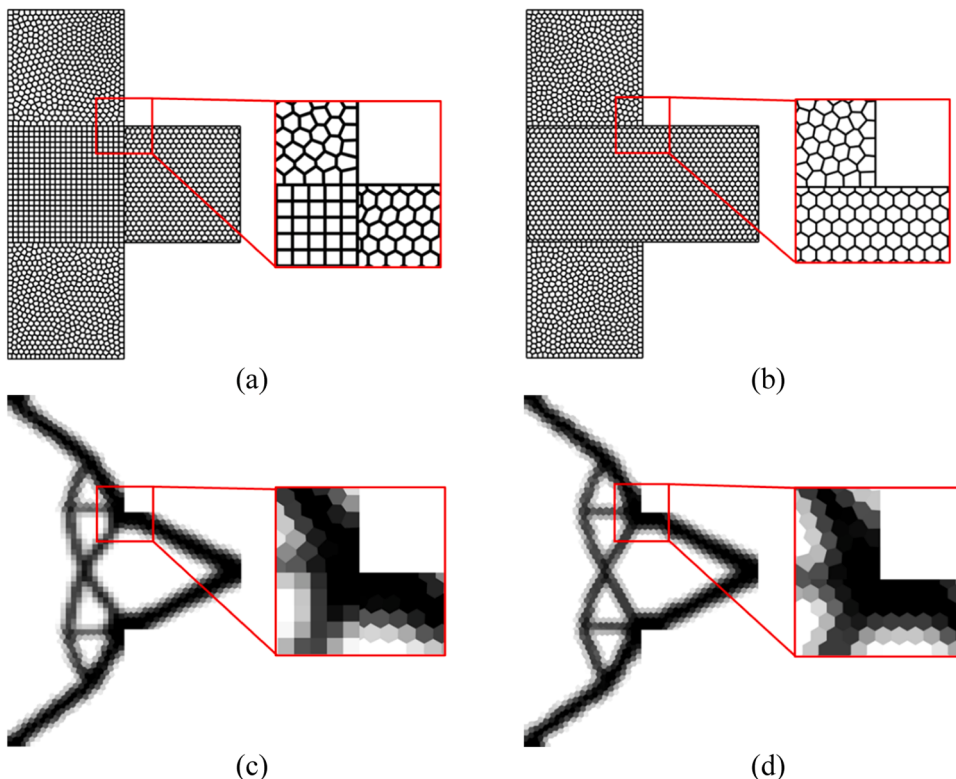


Fig. 13. Different mesh types for multi-domain mesh and corresponding topological configurations.

5.3. Automotive floor frame

To validate the effectiveness of multi-material structural optimization in multi-domain assembly connections, a simplified automotive floor frame was modeled as the optimization design object. As shown in Fig. 14, the design domain has a dimension of $L = 6$. The midpoints of the top, bottom, left, and right boundaries are fixed, and loads of magnitude 0.5 are applied at the specified positions. Additionally, there are two non-designable regions located at both the top and bottom ends of the model. The automotive floor frame is constructed using five domains (Domain 1-Domain 2-Domain 3-Domain 4-Domain 5) connected through the proposed assembly method, as depicted in Fig. 15. The corresponding mesh connection scheme is illustrated in Fig. 16, with the number of mesh elements in each domain being 512-512-2400-874-874. It is important to note that subsequent structural optimization will be conducted based on this mesh connection scheme. The filter radius is set to 1, and the volume fraction is set to 0.4.

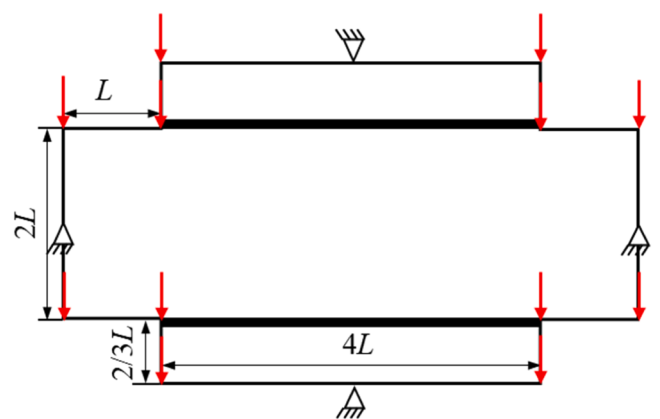


Fig. 14. Schematic diagram of a single-domain automotive floor frame structure.

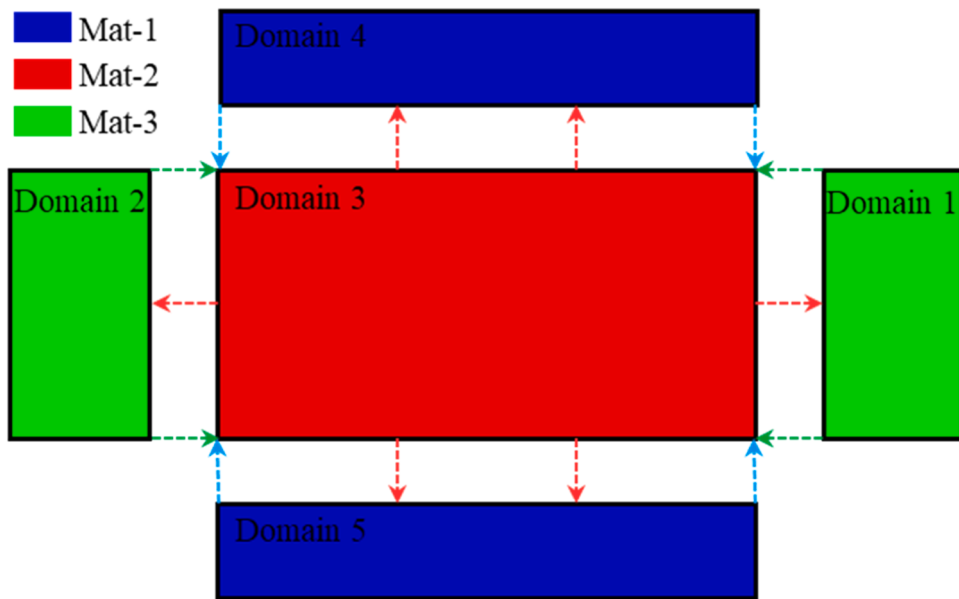


Fig. 15. Schematic diagram of the assembly connection of 5 subdomains.

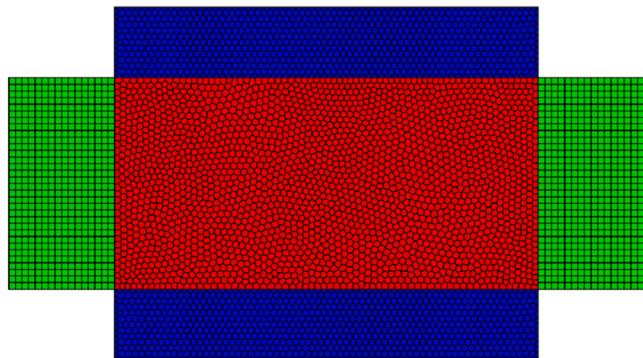


Fig. 16. Mesh connection scheme for the multi-domain assembly.

5.3.1. Multi-material topology optimization

In addition, this example considers three simple anisotropic materials for optimization design. Domains 1 and 2 share the same material, while Domains 4 and 5 share another identical material. The material property parameters for Eq. (2) are assigned as follows: $E_f = 1$, $E_m = 1/15$, $\mu_f = 0.22$, $\mu_f = 0.38$, $G_f = E_f / 2(1 + \mu_f)$, $G_m = E_m / 2(1 + \mu_m)$. Three different materials (Mat1, Mat2, Mat3) with varying fiber volume fractions ($F_{fib} = 0.1/0.6/1$) are employed and represented by three colors: green, blue and red. The elastic matrices of the three materials are shown as follows

$$\begin{aligned} D_{\text{Mat1}} &= \begin{bmatrix} 0.1704 & 0.0285 & 0 \\ 0.0285 & 0.0783 & 0 \\ 0 & 0 & 0.0267 \end{bmatrix}, D_{\text{Mat2}} = \begin{bmatrix} 0.6391 & 0.0439 & 0 \\ 0.0439 & 0.1545 & 0 \\ 0 & 0 & 0.0555 \end{bmatrix}, \\ D_{\text{Mat3}} &= \begin{bmatrix} 1.0509 & 0.2312 & 0 \\ 0.2312 & 1.0509 & 0 \\ 0 & 0 & 0.4098 \end{bmatrix} \end{aligned} \quad (29)$$

Different materials are assigned to each subdomain (Domain 1–Domain 2–Domain 3–Domain 4–Domain 5) for structural topology optimization, as shown in Fig. 17. The table includes eight material assembly schemes, covering single-material multi-domain assemblies,

two-material assemblies, and three-material assemblies. For clarity, three colors are used to represent the materials: green for Mat1, blue for Mat2, and red for Mat3.

As observed from Fig. 17, conducting structural topology optimization for anisotropic, multi-material, and multi-domain assemblies is feasible. Each configuration produces reasonable topologies with well-distributed materials across the subdomains and good continuity at the assembly connections. However, from the perspective of structural support for the automotive floorboard, single-material assembly connections reveal certain shortcomings. When only Mat1 is considered, the top and bottom domains (Domain4 and Domain5) lack sufficient material support. Similarly, when only Mat2 is used, the central domain (Domain3) exhibits significant deficiencies. In contrast, the three topological configurations optimized with two materials effectively mitigate these issues.

Furthermore, topology optimizations with three-material assemblies are explored. We evaluated the following combinations, Option 1: Mat1-Mat1-Mat2-Mat3-Mat3, Option 2: Mat1-Mat1-Mat3-Mat2-Mat2 and Option 3: Mat2-Mat2-Mat3-Mat1-Mat1. Fig. 18 shows the variation of structural compliance with iteration steps for the three assembly schemes. It is worth noting that compliance refers to the overall compliance of the assembled structure consisting of all subdomains. The figure also includes the iteration process for Option 2's topology. The results indicate that the iteration curves converge quickly and steadily, without significant oscillations, demonstrating the algorithm's robustness. Among the three options, Option 2 achieves the best overall performance in terms of the design objective, structural reasonableness, and convergence speed. In contrast, Option 1 results in higher compliance values, and Option 3 exhibits deficiencies in the final topology.

5.3.2. Topology optimization of different element collocation

The studies above are conducted under the assumption of approximately uniform element sizes across subdomains. In practical engineering applications, especially in assembly structures, high-precision subdomains often employ finer meshes, while low-precision subdomains use coarser meshes. This approach balances optimization accuracy and efficiency.

Based on this principle, Option 1 of the three-material assembly are selected for a comparative study to evaluate the influence of different mesh distributions on structural topology. Since the configurations of Domain 1, Domain 2, and Domain 3 remained relatively stable in the

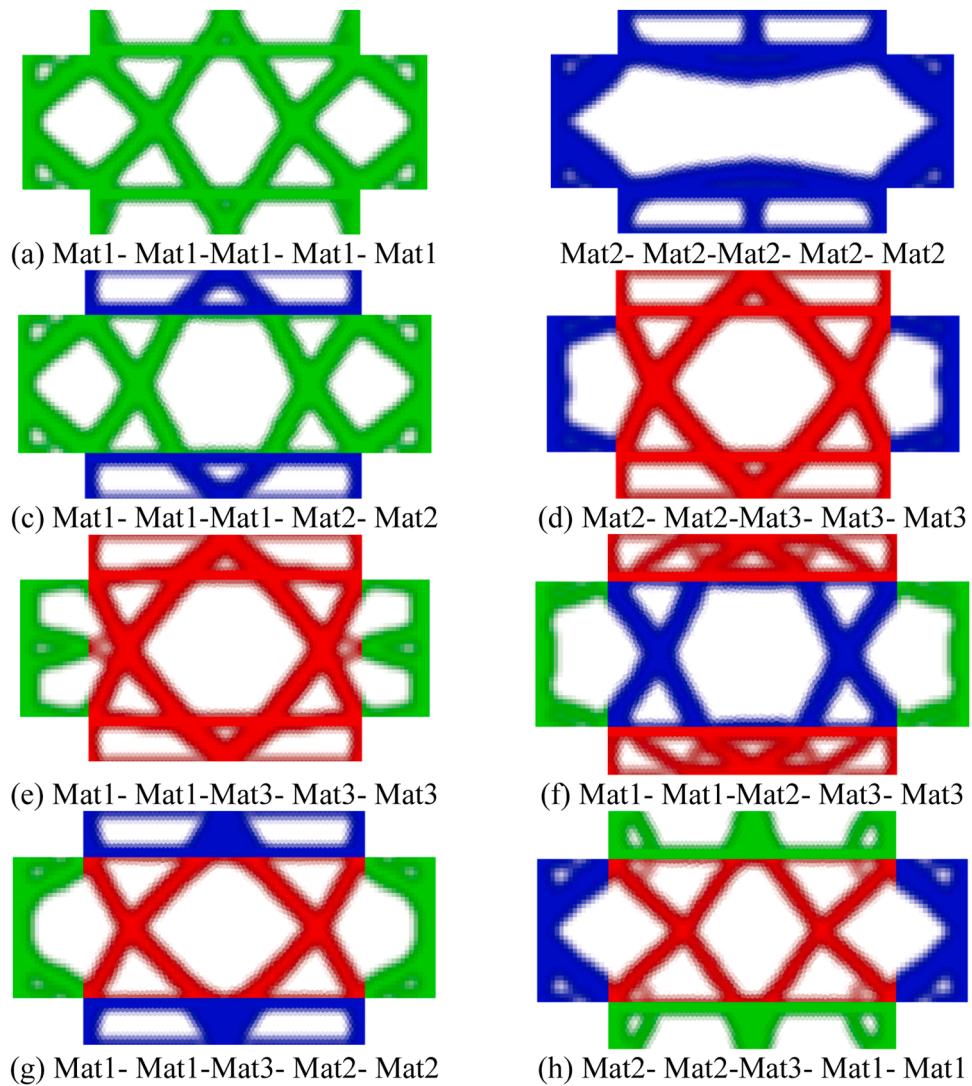


Fig. 17. Topological configurations under various material assembly schemes.

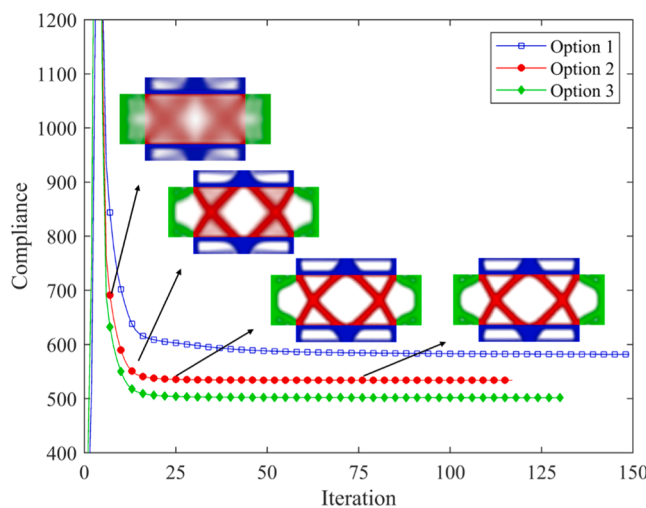


Fig. 18. Compliance iterative curves for three-material assembly connections.

two cases, these domains are treated as low-precision regions with reduced mesh density. Conversely, Domain 4 and Domain 5 are treated as high-precision regions, maintaining their original mesh density. Three mesh distribution schemes (Scheme 1, Scheme 2 and Scheme 3) are defined for Domain 1-Domain 2-Domain 3-Domain 4-Domain 5 as 288-288-2400-874-874, 512-512-2400-1688-1688 and 1152-1152-5000-1688-1688, respectively. The filter radius is adjusted to 0.8 and the other parameters remain unchanged.

The corresponding meshes and topological configurations shown in Table 2. It can be observed that for Scheme 2, which features a mesh assembly with varying element sizes, the method remains feasible. Comparing the three mesh schemes, the topology configurations of Domains 1, 2, and 3 (low-precision domains) exhibit minimal differences, while the configurations of Domains 4 and 5 (high-precision domains) show noticeable variations. In Scheme 1, Domains 4 and 5 lack a distinct support structure.

Table 3 presents the structural compliance and the time consumed at various stages of the optimization process. From the perspective of structural compliance, there is an increasing trend from Scheme 1 to Scheme 3. The increase in iteration time mainly stems from the need to compute the constitutive stiffness of each polygonal element in SBFEM via eigenvalue decomposition (see Eq. (13) for details). In high-resolution meshes, the computational cost of eigenvalue solving rises significantly. Although the increase in element number improves

Table 2

Meshes and topological configurations under different schemes.

	Mesh	Topology
Scheme 1		
Scheme 2		
Scheme 3		

Table 3

Structural compliance and time of each stage under different schemes.

	Compliance	Time			Sum
		Mesh	Analysis	Optimization	
Scheme 1	544.43	6.44	2.07	13.95	22.46
Scheme 2	547.76	8.77	2.66	17.36	28.79
Scheme 3	569.44	11.32	4.16	24.68	40.16

solution accuracy, it also leads to higher compliance values (i.e., larger displacements). In combination with the topology configuration, from the point of view of time, Scheme 2 strikes a balance by employing low-density meshes in low-precision domains, thereby significantly reducing the overall optimization time while maintaining topology integrity.

The adaptive mesh resolution study provides compelling evidence of the framework's computational efficiency and practical scalability. By strategically allocating finer meshes to high-stress regions while maintaining coarser discretization in less critical areas, the method achieves an optimal balance between accuracy and computational cost. The balanced Scheme 2 configuration delivers nearly identical topological features to the high-resolution Scheme 3 while reducing total computation time by 28. This highlights the method's potential for large-scale engineering applications. However, we also acknowledge possible computational bottlenecks in such scenarios.

5.4. Building structure

A truncated elliptical building structure with dimensions $H = 15$ and $L = 30$, as shown in Fig. 19(a), is utilized to study the impact of sub-domain volume constraints on structural optimization. The design domain consists of five subdomains (Domain 1–Domain 2–Domain 3–Domain 4–Domain 5), with non-designable regions introduced at the boundaries between Domain 2, Domain 3, Domain 4, and Domain 5. The corresponding mesh assembly connection scheme for each subdomain is shown in Fig. 19(b), in which non-uniform polygonal mesh and approximated polygonal mesh with honeycomb feature are selected, and subdomains' mesh numbers are 800, 1745, 1500, 2084, and 1500, respectively, represented in magenta, yellow, green, blue, and red. Since

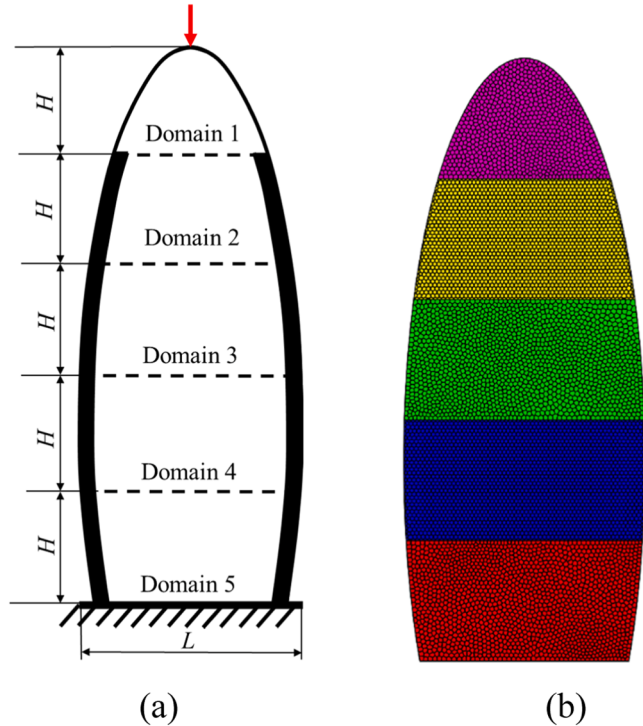


Fig. 19. The building structure, (a) the design domain and (b) the mesh assembly connection.

this example primarily focuses on the effects of constraints, all sub-domains are modeled using the same isotropic material with an elastic modulus $E = 1$ and a Poisson's ratio $\mu = 0.3$. Constraints are applied at the bottom of the design domain, and a force of magnitude 1 is applied at the top. The filter radius is set to 1.

Table 4 shows the optimized configurations under various volume constraint ratios. It is worth noting that, as this example addresses a multi-constraint problem, the ZPR optimization scheme has been

Table 4

Optimized configurations and compliance values under different volume constraint ratios.

Volume ratios	0.5-0.5-0.5-0.5-0.5	0.45-0.35-0.4-0.55-0.75	0.6-0.45-0.4-0.45-0.6	0.5
Configurations				
Compliance	8.732	10.96	8.85	7.25

employed. To facilitate observation, the five previously mentioned colors are used to represent the topology of each subdomain in the optimization results.

From the above table, it can be observed that the proposed multi-domain assembly-connected structural topology optimization method is equally applicable to multi-constraint scenarios. Under different volume ratios, the structural topologies exhibit noticeable variations. When the volume constraint for Domain 1 is greater than or equal to 0.5 (e.g., 0.5 or 0.65), material support is generated in the middle of Domain 1, which extends through Domain 2, forming branches in Domain 3 that connect to Domains 4 and 5. In contrast, when the volume fraction is 0.45, the support originates in Domain 2. Based on the structural compliance values, it is evident that a higher material proportion in the subdomains closer to the top load results in better structural performance. For a more direct comparison, we also provide the topology of a single-domain structure under a single constraint. It can be observed that the material is more concentrated near the top load location.

Crucially, the framework maintains compatibility between non-uniform polygonal and honeycomb meshes while respecting non-designable boundaries, proving its versatility for architectural applications. Compared to single-domain optimization, this approach expands design flexibility by allowing engineers to strategically redistribute material across subdomains without remeshing. Designers can tailor their design goals by assigning different constraints to meet their specific needs, demonstrating excellent potential for practical engineering applications.

6. Conclusions

This study presents a novel integrated optimization framework for multi-domain assemblies, addressing the critical challenges of geometric complexity, material heterogeneity, and localized load demands in practical engineering structures. The proposed framework combines the SBFEM with the SIMP approach to enable seamless integration of non-matching meshes and diverse material properties across subdomains. Key contributions of this work include:

- Assembly-Oriented SBFEM implementation: The framework leverages SBFEM's polygonal element analysis capabilities to enforce compatibility at interfaces without remeshing, preserving mechanical equilibrium across dissimilar meshes. The automatic generation

of polygonal transition elements at junctions ensures smooth load-path continuity.

- Subdomain-Specific optimization: By allowing independent meshing and material assignment for each subdomain, the method accommodates localized design requirements while maintaining global structural performance. The integration of anisotropic and isotropic material models further enhances flexibility.
- Computational efficiency: Adaptive mesh strategies and the elimination of iterative remeshing significantly reduce computational overhead, as demonstrated in numerical examples such as the automotive floor frame and building structure.
- Robustness and versatility: Numerical experiments validate the framework's effectiveness in handling variable mesh densities, multi-material interfaces, and complex geometries. The method achieves consistent performance across different assembly configurations and constraint scenarios.

The proposed framework bridges the gap between single-domain topology optimization and practical multi-component assembly design, providing a unified workflow from mesh assembly to optimized design. While the method shows great promise, several limitations remain. Currently, it is restricted to two-dimensional linear elastic problems, and the SBFEM requires the scaling center visibility condition, which may necessitate subdivision of certain concave polygons. Additionally, multi-domain coupling only enforces displacement continuity and does not yet handle normal stress constraints at interfaces. Extending the framework to three-dimensional structures holds significant potential but also introduces challenges such as increased computational complexity and more complex geometry representation. Addressing these limitations in future work will broaden the method's applicability to more complex and realistic engineering problems. Overall, this approach offers a promising pathway for advancing high-performance engineering system design in fields including automotive, aerospace, and civil engineering.

CRediT authorship contribution statement

Xinqing Li: Writing – original draft, Validation, Software, Methodology, Conceptualization. **Jianghong Yang:** Writing – original draft, Validation, Software, Methodology. **Mi Xiao:** Writing – review & editing, Methodology. **Yingjun Wang:** Writing – review & editing,

Supervision, Methodology, Conceptualization.

CRediT authorship contribution statement

Xinqing Li: Writing – original draft, Validation, Software, Methodology, Conceptualization. **Jianghong Yang:** Writing – original draft, Validation, Software, Methodology. **Mi Xiao:** Writing – review & editing, Methodology. **Yingjun Wang:** Writing – review & editing, Supervision, Methodology, Conceptualization.

Declaration of competing interest

The authors declare that they have no known competing financial interests or personal relationships that could have appeared to influence the work reported in this paper.

Acknowledgments

This work has been supported by the Guangdong Basic and Applied Basic Research Foundation (2024A1515011786 and 2025A1515010672).

Data availability

Data will be made available on request.

References

- [1] Wang K, Zhu W, Yang L, Gu X, Guo L. Position and orientation estimation method based on 3D digital morphology contour registration. *Meas Sci Technol* 2024;36:015203.
- [2] Zhang Y, Fan X. Assembly building structure simulation method based on 3D simulation technology, frontier computing. Singapore: Springer Singapore; 2020. p. 1260–6.
- [3] Zhuang C, Liu Z, Liu J, Ma H, Zhai S, Wu Y. Digital twin-based quality management method for the assembly process of aerospace products with the Grey-Markov model and Apriori algorithm. *Chin J Mech Eng* 2022;35:105.
- [4] Bendsoe MP, Kikuchi N. Generating optimal topologies in structural design using a homogenization method. *Comput Methods Appl Mech Eng* 1988;71:197–224.
- [5] Wang Y, Li X, Long K, Wei P. Open-source codes of topology optimization: a summary for beginners to start their research. *CMES - Comput Model Eng Sci* 2023;137:1–34.
- [6] Liu C-H, Huang G-F, Chen T-L. An evolutionary soft-add topology optimization method for synthesis of compliant mechanisms with maximum output displacement. *J Mech Robot* 2017;9:054502.
- [7] Kambayashi K, Kogiso N, Watanabe I, Yamada T. Level-set-based topology optimization of a morphing flap as a compliant mechanism considering finite deformation analysis. *Struct Multidisc Optim* 2023;66:223.
- [8] Zhang S, Da D, Wang Y. TPMS-infill MMC-based topology optimization considering overlapped component property. *Int J Mech Sci* 2022;235:107713.
- [9] Jiang T, Chirehdast M. A systems approach to structural topology optimization: designing optimal connections. *J Mech Des* 1997;119:40–7.
- [10] Chickermane H, Gea HC. Design of multi-component structural systems for optimal layout topology and joint locations. *Eng Comput* 1997;13:235–43.
- [11] Li Q, Steven GP, Xie YM. Evolutionary structural optimization for connection topology design of multi-component systems. *Eng Comput (Swansea)* 2001;18:460–79.
- [12] Yildiz AR, Saitou K. Topology synthesis of multicomponent structural assemblies in continuum domains. *J Mech Des* 2011;133:011008.
- [13] Zhou Z, Hamza K, Saitou K. Decomposition templates and joint morphing operators for genetic algorithm optimization of multicomponent structural topology. *J Mech Des* 2013;136:021004.
- [14] Guirguis D, Hamza K, Aly M, Hegazi H, Saitou K. Multi-objective topology optimization of multi-component continuum structures via a Kriging-interpolated level set approach. *Struct Multidisc Optim* 2015;51:733–48.
- [15] Guirguis D, Aly MF. An evolutionary multi-objective topology optimization framework for welded structures. In: 2016 IEEE Congress on Evolutionary Computation; 2016. p. 372–8.
- [16] Sigmund O. On the usefulness of non-gradient approaches in topology optimization. *Struct Multidisc Optim* 2011;43:589–96.
- [17] Zhou Y, Saitou K. Gradient-based multi-component topology optimization for stamped sheet metal assemblies (MTO-S). *Struct Multidisc Optim* 2018;58:83–94.
- [18] Zhou Y, Saitou K. Gradient-based multi-component topology optimization for additive manufacturing (MTO-A). In: 43rd Design Automation Conference; 2017. V02AT03A033.
- [19] Zhou Y, Nomura T, Saitou K. Multi-component topology and material orientation design of composite structures (MTO-C). *Comput Methods Appl Mech Eng* 2018;342:438–57.
- [20] Zhou H, Zhang J, Zhou Y, Saitou K. Multi-component topology optimization for die casting (MTO-D). *Struct Multidisc Optim* 2019;60:2265–79.
- [21] Zhang J, Wang S, Zhou H, Ning L. Multi-component topology optimization for thin-walled structures. *Eng Optimizat* 2022;54:847–63.
- [22] Zhu J, Zhang W, Beckers P. Integrated layout design of multi-component system. *Int J Numer Methods Eng* 2009;78:631–51.
- [23] Qiao Z, Weihong Z, Jihong Z, Tong G. Layout optimization of multi-component structures under static loads and random excitations. *Eng Struct* 2012;43:120–8.
- [24] Zhu J-H, Guo W-J, Zhang W-H, Liu T. Integrated layout and topology optimization design of multi-frame and multi-component fuselage structure systems. *Struct Multidisc Optim* 2017;56:21–45.
- [25] Bao J, Liu P, Zhong J, Xu Y, Luo Y. Surrogate-based integrated design of component layout and structural topology for multi-component structures. *Struct Multidisc Optim* 2023;66:26.
- [26] Thomas S, Li Q, Steven G. Topology optimization for periodic multi-component structures with stiffness and frequency criteria. *Struct Multidisc Optim* 2020;61:2271–89.
- [27] Ambrozkiewicz O, Kriegsmann B. Simultaneous topology and fastener layout optimization of assemblies considering joint failure. *Int J Numer Methods Eng* 2021;122:294–319.
- [28] Ferro R, Pavanello R. Sequential method of topological optimization in multi-component systems. *Lat Am J Solids Struct* 2023;20:501.
- [29] Francavilla A, Zienkiewicz OC. A note on numerical computation of elastic contact problems. *Int J Numer Methods Eng* 1975;9:913–24.
- [30] Xing W, Song C, Tin-Loi F. A scaled boundary finite element based node-to-node scheme for 2D frictional contact problems. *Comput Methods Appl Mech Eng* 2018;333:114–46.
- [31] Talisch C, Paulino GH, Pereira A, Menezes IFM. PolyTop: a Matlab implementation of a general topology optimization framework using unstructured polygonal finite element meshes. *Struct Multidisc Optim* 2012;45:329–57.
- [32] Sanders ED, Pereira A, Aguiló MA, Paulino GH. PolyMat: an efficient Matlab code for multi-material topology optimization. *Struct Multidisc Optim* 2018;58:2727–59.
- [33] Giraldo-Londoño O, Paulino GH. PolyDyna: a Matlab implementation for topology optimization of structures subjected to dynamic loads. *Struct Multidisc Optim* 2021;64:957–90.
- [34] Giraldo-Londoño O, Paulino GH. PolyStress: a Matlab implementation for local stress-constrained topology optimization using the augmented lagrangian method. *Struct Multidisc Optim* 2021;63:2065–97.
- [35] Egger AW, Saputra A, Triantafyllou SP, Chatzis E. Exploring topology optimization on hierarchical meshes by scaled boundary finite element method. In: 10th International Conference on Computational Methods (ICCM 2019), Singapore, Singapore, July 9–13, 2019. Scientechn Publisher LLC; 2019. p. 492.
- [36] Zhang W, Xiao Z, Liu C, Mei Y, Youn S-k, Guo X. A scaled boundary finite element based explicit topology optimization approach for three-dimensional structures. *Int J Numer Methods Eng* 2020;121:4878–900.
- [37] Gao G, Yang J, Li X, Gu J, Wang Y. Fluid topology optimization using quadtree-based scaled boundary finite element method. *Eng Anal Bound Elem* 2024;169:106019.
- [38] Su R, Boonlertnirun P, Tangaramvong S, Song C. Isosurface-based marching cube algorithm for smooth geometric topology optimization within adaptive octree SBFE approach. *Eng Anal Bound Elem* 2024;168:105920.
- [39] Su R, Tangaramvong S, Song C. Automatic image-based SBFE-BESO approach for topology structural optimization. *Int J Mech Sci* 2024;263:108773.
- [40] Su R, Zhang X, Tangaramvong S, Song C. Adaptive scaled boundary finite element method for two/three-dimensional structural topology optimization based on dynamic responses. *Comput Methods Appl Mech Eng* 2024;425:116966.
- [41] Ooi ET, Song C, Tin-Loi F. A scaled boundary polygon formulation for elasto-plastic analyses. *Comput Methods Appl Mech Eng* 2014;268:905–37.
- [42] Li X, Su H, Wang Y. An improved polygon mesh generation and its application in SBFE using NURBS boundary. *Comput Mech* 2024.
- [43] Lu Y, Tong L. Concurrent topology optimization of cellular structures and anisotropic materials. *Comput Struct* 2021;255:106624.
- [44] Talisch C, Paulino GH, Pereira A, Menezes IFM. PolyMesher: a general-purpose mesh generator for polygonal elements written in Matlab. *Struct Multidisc Optim* 2012;45:309–28.
- [45] Ooi ET, Song C, Tin-Loi F, Yang Z. Polygon scaled boundary finite elements for crack propagation modelling. *Int J Numer Methods Eng* 2012;91:319–42.
- [46] Song C, Wolf JP. The scaled boundary finite-element method—Alias consistent infinitesimal finite-element cell method—for elastodynamics. *Comput Methods Appl Mech Eng* 1997;147:329–55.
- [47] Li X, Su H, Yang J, Gao G, Wang Y. NURBS-boundary-based quadtree scaled boundary finite element method study for irregular design domain. *Eng Anal Bound Elem* 2024;159:418–33.
- [48] Zhang XS, Paulino GH, Ramos AS. Multi-material topology optimization with multiple volume constraints: a general approach applied to ground structures with material nonlinearity. *Struct Multidisc Optim* 2018;57:161–82.